# Study of EPR-based nanodielectrics under operational conditions for DC cable insulation

Cite as: J. Appl. Phys. **132**, 084101 (2022); https://doi.org/10.1063/5.0091930 Submitted: 18 March 2022 • Accepted: 05 August 2022 • Published Online: 22 August 2022

🧓 Mohamadreza Arab Baferani, 🗓 Tohid Shahsavarian, 🗓 Mattewos Tefferi, et al.

















# Study of EPR-based nanodielectrics under operational conditions for DC cable insulation

Cite as: J. Appl. Phys. 132, 084101 (2022); doi: 10.1063/5.0091930

Submitted: 18 March 2022 · Accepted: 5 August 2022 ·

Published Online: 22 August 2022







Mohamadreza Arab Baferani,<sup>1,2</sup> D Tohid Shahsavarian,<sup>1,2</sup> D Mattewos Tefferi,<sup>1,2</sup> D Qin Chen,<sup>3</sup> and Yang Cao<sup>1,2,a)</sup>

#### **AFFILIATIONS**

- <sup>1</sup>Department of Electrical and Computer Engineering, University of Connecticut, Storrs, Connecticut 06269, USA
- <sup>2</sup>Electrical Insulation Research Center, Institute of Material Science, University of Connecticut, Storrs, Connecticut 06269, USA
- <sup>3</sup>GE Global Research Center, Niskayuna, New York 12309, USA

#### **ABSTRACT**

A model DC material based on ethylene propylene rubber (EPR) including the pure EPR and the EPR-based nanodielectrics incorporated with two different nanoclays, Kaoline and Talc, under operational conditions was investigated. The operational conditions include a 20 kV/mm electric field at 25 °C, a 20 kV/mm electric field at 50 °C with a thermal gradient, and a 40 kV/mm electric field at 50 °C with a thermal gradient and polarity reversal. Space charge distribution, surface potential, and electrical conductivity were measured to characterize the model DC material and interpret the discrete charge dynamics in the bulk and at the interface of the three samples. The experimental results revealed that the electrical conductivity of Talc-filled nanodielectric has the least dependency on electric field and temperature, which reduces the conductivity gradient across the dielectric. Moreover, the successful suppression of space charge and the lower dielectric time constant in the Talc-filled nanodielectric result in a tuning electric field in the bulk not only under normal operating conditions but also more importantly under polarity reversal conditions. The maximum of absolute charge density decreases from 10.6 C/m³ for EPR to 2.9 C/m³ for the Talc-filled nanodielectric under 40 kV/mm with polarity reversal and at 50 °C with the thermal gradient. The maximum of local electric field enhancement for the mentioned condition reduces significantly from 97 kV/mm, 142% enhancement, for EPR to 45 kV/mm, only 12.5% enhancement, for the Talc-filled nanodielectric.

Published under an exclusive license by AIP Publishing. https://doi.org/10.1063/5.0091930

#### I. INTRODUCTION

The extension of power grids' interconnection with an increased amount of power flow control, the integration of distributed energy resources (DER), and the long-distance transmission and integration of large blocks of wind, solar, and hydro powers all call for the accelerated development of high-voltage direct current (HVDC) transmission. Lower power loss, higher capacity for a fixed corridor, fully controllable power flow, better transmission and stabilization capabilities between non-synchronized AC power systems, and no length restriction because of free of charging current or reactive power compensation mark the advantages of HVDC transmission over high-voltage alternating current (HVAC) transmission. For power transmission across the wide metropolitan areas or for island or off-shore wind farm interconnections, HVDC cables as either underground or submarine cabling are indispensable needs. Lo

Tuning the electric field in HVDC cable insulation remains challenging in comparison to HVAC cable insulation, which has capacitive field grading with dielectric constant not dependent on the electric field and temperature.<sup>7,8</sup> The electric field grading in HVDC cable insulation is resistive field grading governed by electrical conductivity that is strongly dependent on the electric field and temperature. 9,10 Therefore, electric field distribution in HVDC cable insulation that initially follows Laplacian field distribution in no-load condition undergoes inevitably a "field inversion" toward the full-load condition. 11,12 In this regard, the presence of space charge across the extruded HVDC cable with polymeric insulation can distort electric field distribution with a local electric field enhancement across insulation that accelerates the degradation and aging of insulation.<sup>13</sup> Moreover, the transient electric field distortion during and shortly after polarity reversal (PR) in power systems using traditional current source converter (CSC)

<sup>&</sup>lt;sup>a)</sup>Author to whom correspondence should be addressed: yang.cao@uconn.edu. Tel.: (860) 486-0915

technology would be worsened by space charge accumulation. As a result, extruded polymeric cables have been used only in HVDC power transmission based on voltage source converter (VSC) technology that does not need the change of voltage polarity to reverse the power flow direction.<sup>3</sup> Therefore, suppression of space charge and the controlling electric field under different operational conditions including PR in polymeric dielectrics used for extruded HVDC cable insulation is still an essential need and requirement.

Ethylene propylene rubber (EPR) has many advantages over cross-linked polyethylene (XLPE) such as higher flexibility, reduced thermal expansion, and lower sensitivity to water treeing. 14,15 However, the pure EPR does not have proper dielectric properties, and it should be tailored for HVDC cable insulation. Incorporating nanoparticle fillers can improve the dielectric properties of polymeric insulation, especially space charge suppression for a better performance of polymeric insulation. 17-23 The suppression effect in all the previous studies<sup>17-23</sup> is based on introduced deep traps for efficient charge capturing near the electrode-dielectric interface so as to reduce the electric field next to the electrode to block charge injection. These approaches are inherently prone to voltage PR and may lead to insulation failure in emerging Smart-Grids with topologies like multi-terminal DC designed for distributed, clean, and renewable energies integration. Our novel approach of trap modulation is based on shallow traps introduced by incorporating large interface two-dimensional (2D) nanoclay in polymer dielectrics with superior DC characteristics. The behavior of the introduced DC model material for HVDC cable insulation in terms of space charge accumulation, tuning electric field, and controlling the transient electric field during and after polarity reversal is investigated under different operational conditions. In addition, the charge dynamics behavior of the model material is characterized and interpreted using surface potential measurement along with the space charge measurement.

#### **II. MODEL AND METHODOLOGY**

#### A. Sample preparation

Three different samples with ethylene propylene rubber (EPR) as the base polymer and peroxide as the cross-linker agent were studied. The first sample is the pure EPR named with EPR. The second one is EPR with 40% Kaolinite nanoparticles, which is labeled as EPR-K. The third sample is EPR with 40% Talc nanoparticles presented as EPR-T in this paper. The samples were hotpressed at 120 °C and under 9 tons pressure into a plaque with a desired thickness. Then, the samples were cross-linked at 165 °C and under 5 tons pressure. All the samples were degassed at 80 °C for five days after preparation.

#### B. Space charge configuration

The pulsed electroacoustic (PEA) setup shown schematically in Fig. 1 was used to measure the charge distribution across the thickness of plaque samples. <sup>24</sup> The plague samples with the thickness of  $\sim\!250\,\mu\mathrm{m}$  were metalized on both sides with 60/40% gold/palladium. The whole setup of PEA was housed inside an oven to control the ambient temperature. Four small heaters were placed on the bottom electrode to provide the thermal gradient (TG) of 1.2 °C/mm across the thickness of the sample parallel with the applied electric field to simulate the load condition in a power cable. The temperature of the bottom electrode is controlled by changing the heater current. A feedback loop was provided for

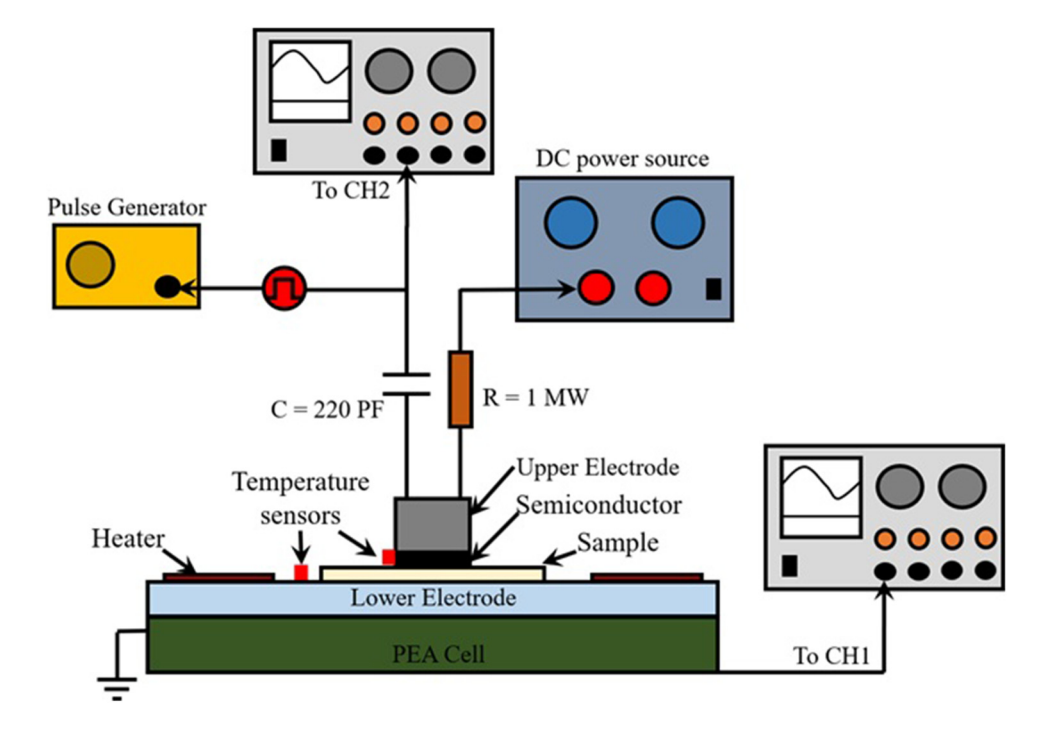


**FIG. 1.** The schematic diagram of the PEA setup.

proportional-integral-derivative (PID) temperature control by deploying a resistor temperature detector (RTD) sensor to monitor the temperature on both upper and lower surfaces of the specimen.

#### C. Surface potential configuration

Surface potential under two different scenarios was measured using a Kelvin type probe (model number 6000B-5C, Trek) linked with an electrostatic voltmeter (model number 347, Trek).<sup>25</sup>

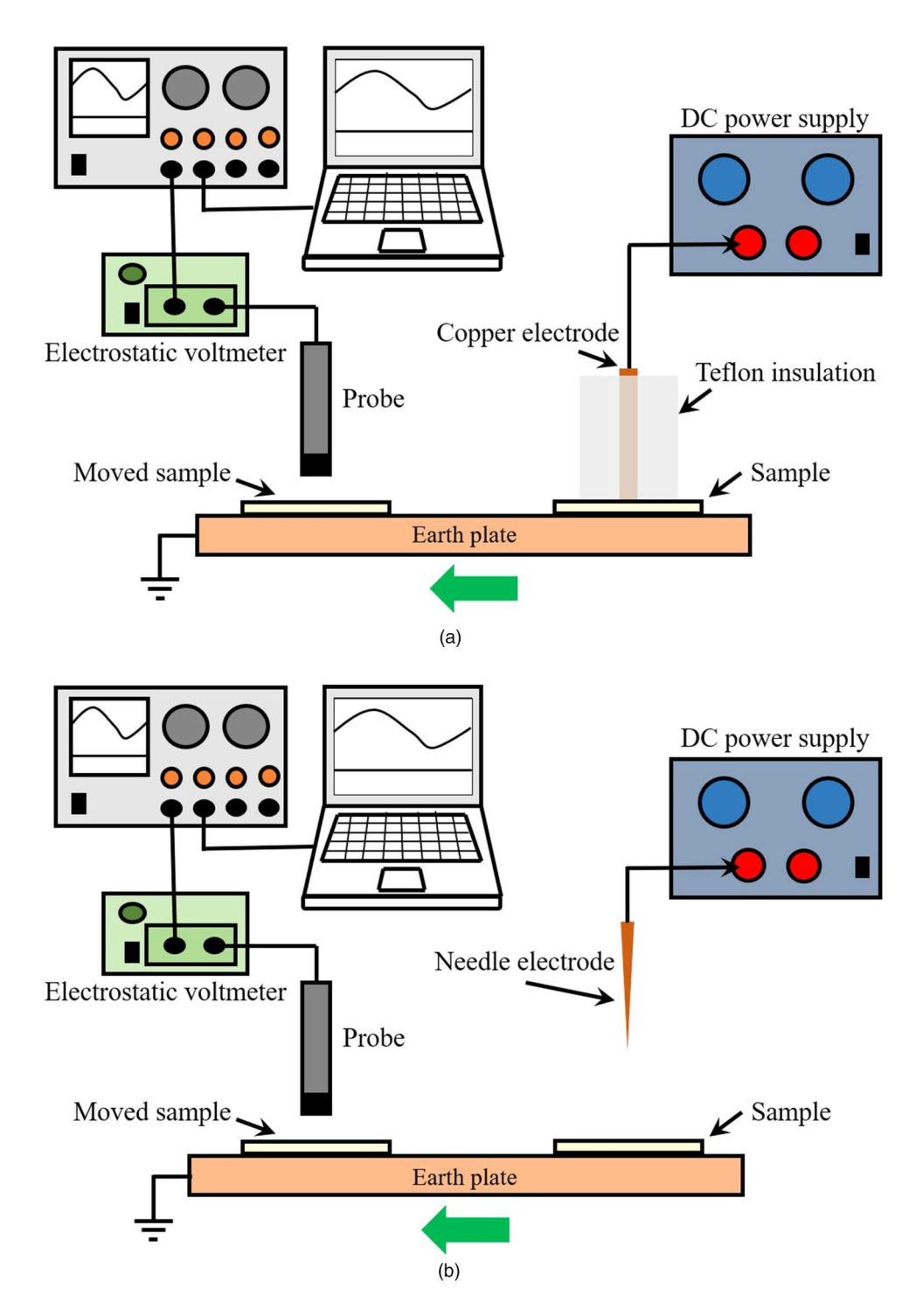


FIG. 2. The schematic diagram of surface potential measurement (a) under a constant DC electric field charging and (b) under corona charging.

In the first scenario, the samples were polarized under a constant DC electric field with a cylindrical electrode as presented in Fig. 2(a). The copper electrode with a diameter of 1 cm was encapsulated within Teflon with an outer diameter of 4 cm. In the second scenario, the samples were corona charged by a needle electrode over a defined distance above the surface of the sample, as shown in Fig. 2(b). For surface potential measurement, the samples with a dimension of  $5 \times 5$  cm<sup>2</sup> were put below the probe where the distance between the probe and the sample surface is 3 mm.

#### D. Electrical conductivity configuration

DC electrical conductivities of the bulk for the samples were measured using a three-terminal sample holder designed according to ASTM 257 Standard and a Keithley 6514 electrometer. The samples were placed inside an oven to keep the desired temperature, and the conduction current was recorded during 1000 s. An average quasi-steady-state value from 900 to 1000 s of the measurement was used to obtain the electrical conductivity. Samples with a thickness of 200  $\mu \rm m$  were used for electrical conductivity measurement.

#### E. Permittivity measurement

The relative permittivity was measured using the IMASS time domain dielectric spectrometer (TDDS). The TDDS measurements were performed utilizing a stainless-steel guarded electrode configuration with an electrode diameter of 4 cm. The samples were prepared with the thickness of  $\sim 1$  mm, and the test was performed at different temperatures including 25, 50, 75, and 100 °C inside an oven for isothermal measurement.

#### III. EXPERIMENTAL RESULTS

## A. Space charge profile and electric field distribution under 20 kV/mm and at 25 $^{\circ}$ C

Figure 3 presents the results of charge distribution and electric field distribution across the thickness of the three samples under 20 kV/mm at 25 °C for 120 min. The color map demonstrates the time evolution of space charge distribution, with the vertical axis for position across the sample cross section in per unit (P.U.), the horizontal axis for the duration of space charge measurement in minutes, and the color for charge density in C/m³. The EPR sample presents the formation of the trapped hetero-polar charges next to both anode and cathode after their injection and transport

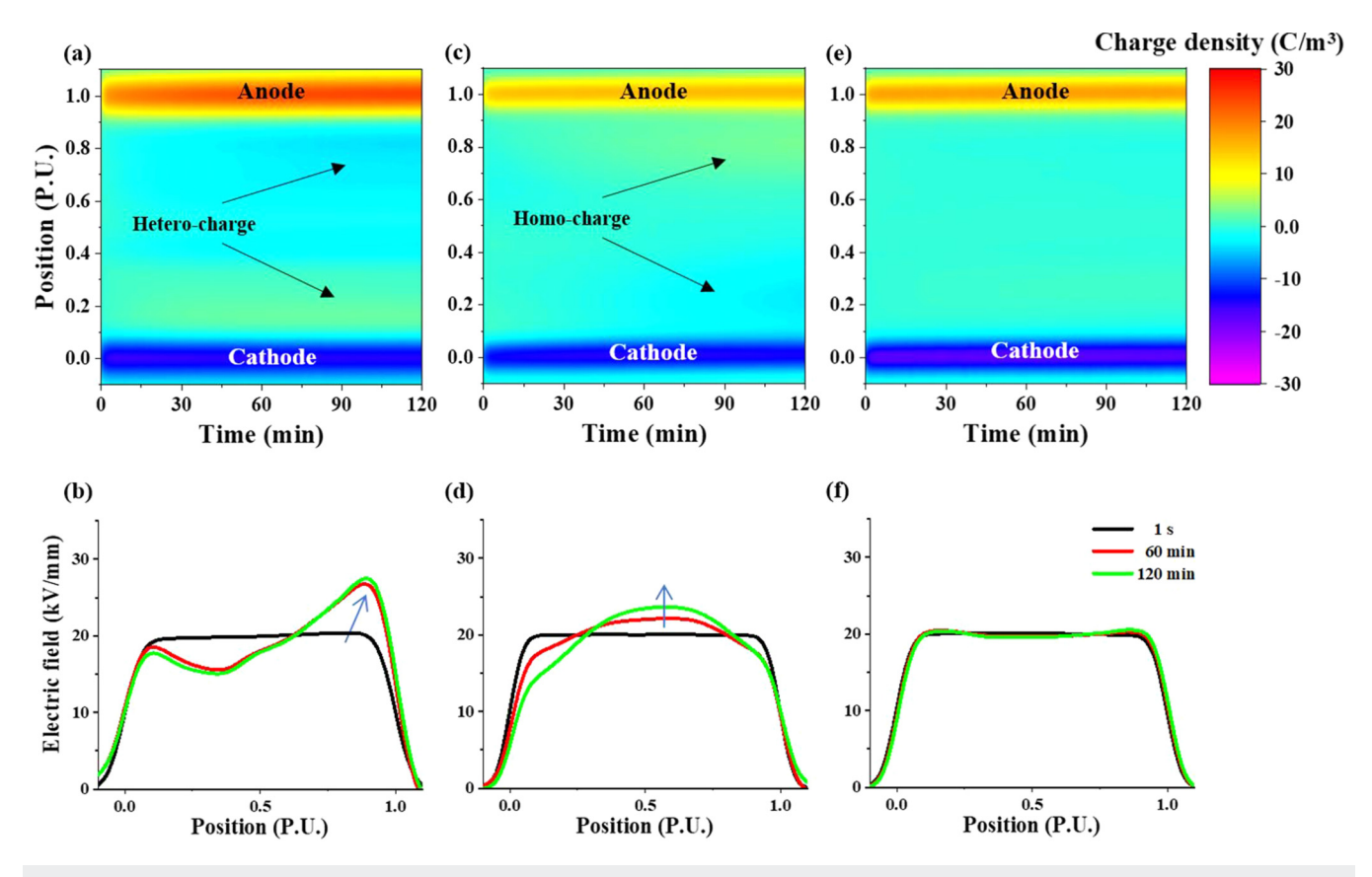


FIG. 3. Charge distribution profile and the resulted electric field distribution at 20 kV/mm and 25 °C for (a) and (b) EPR, (c) and (d) EPR-K, and (e) and (f) EPR-T.

across the dielectric as shown in Fig. 3(a). The charge accumulation initiated from the first minute and increased significantly along the sample especially near the anode after 45 min. For charges at electrode–dielectric interfaces, the amount of injected charges from the cathode is higher. The injected charges moved across the dielectric under the applied voltage and accumulated mainly near the anode. Applying Gauss's law on space charge distribution, the electric field distribution of the EPR sample can be obtained as shown in Fig. 3(b). The higher amount of accumulated negative charges next to the anode along with positive charges at the anode–dielectric interface results in a local electric field enhancement at the interface of the anode. The maximum electric field enhancement reached 26.5 kV/mm next to the anode, which is 32.5% enhancement compared with the nominal electric field of 20 kV/mm.

Under the same electric field and thermal condition, EPR-K showed accumulation of homo-polar charges next to both electrodes as presented in Fig. 3(c). The injected charges from both electrodes were accumulated close to the homo-polar electrode. Thus, the electric field distribution due to charge distribution across the sample is distorted with a local electric field enhancement in the center of the sample [Fig. 3(d)]. The maximum electric field increased to 24 kV/mm, which is 20% field enhancement after 120 min. On the other hand, as it can be seen in Fig. 3(e), the

amount of charge accumulation across the thickness of EPR-T is negligible, which leads to a uniform electric field distribution of about  $20\,\mathrm{kV/mm}$ , as shown in Fig. 3(f), without any local electric field enhancement.

# B. Space charge profile and electric field distribution under 20 kV/mm and at 50 $^{\circ}$ C with TG

The charge profile and the electric field distribution of the samples at 50 °C in the presence of TG across the thickness of the samples are presented in Fig. 4. As mentioned before, the bottom electrode that is a cathode has higher temperature, and the direction of the electric field is in the opposite direction with TG. In Fig. 4(a) of the charge profile of EPR, the injected positive charges from the anode moving toward the cathode under applied voltage were captured across the sample and closer to the cathode. The higher amount of charges near the cathode leads to the local electric field enhancement of up to 28 kV/mm, a 40% enhancement, in the neighborhood of the cathode–dielectric interface as shown in Fig. 4(b). Compared with the same electric field at 25 °C and without TG, the injected charges were accumulated majorly across the dielectric and the maximum electric field was next to the cathode.

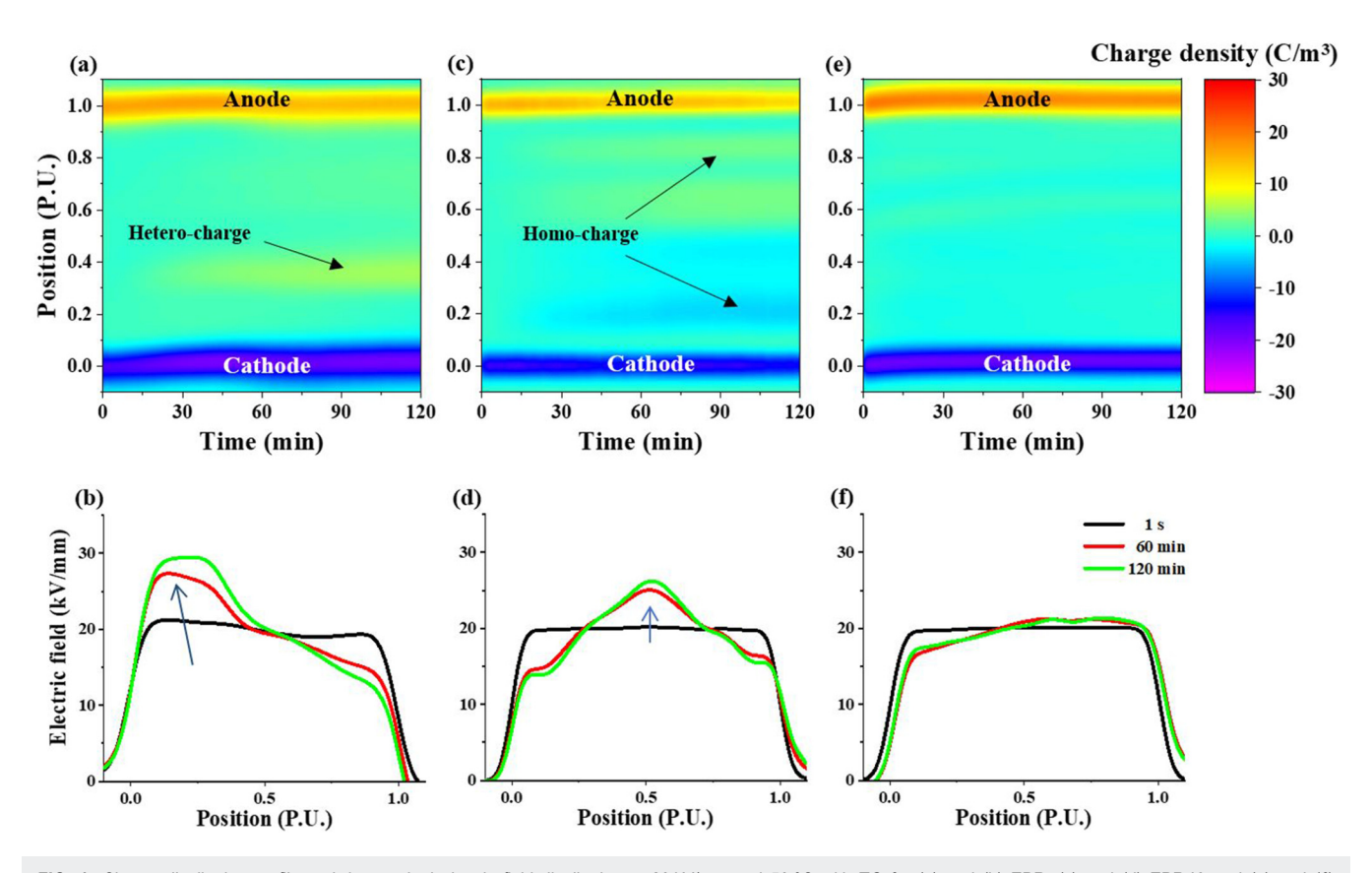


FIG. 4. Charge distribution profile and the resulted electric field distribution at 20 kV/mm and 50 °C with TG for (a) and (b) EPR, (c) and (d) EPR-K, and (e) and (f) EPR-T.

The trend of charge accumulation as homo-polar charges in EPR-K at 50 °C with TG shown in Fig. 4(c) is closely similar to 25 °C. The difference is the amount of accumulated charges that increased with temperature rise and TG. Because of the accumulated homo-polar charges in the bulk next to both electrodes, the obtained electric field distribution as shown in Fig. 4(d) is not uniform, with a local electric field enhancement in the middle of the sample. The maximum electric field raised to  $26\,\mathrm{kV/mm}$ , a 30% enhancement, after 120 min. Under the same condition for EPR-T, a tiny amount of injected charges was accumulated in the bulk, which is shown in Fig. 4(e). The accumulated charges result in electric field distribution with the maximum electric field near the anode of  $21.5\,\mathrm{kV/mm}$ , which is merely a 7.5% enhancement as presented in Fig. 4(f).

# C. Space charge profile and electric field distribution under 40 kV/mm with PR and at 50 $^{\circ}$ C with TG

Figure 5 shows the charge profile and electric field distribution of the samples with the electric field increased to 40 kV/mm and PR after 90 min. During the first cycle over the first 90 min, the injected positive charges from the anode were accumulated across

the EPR sample as seen in Fig. 5(a). The charge accumulation initiated from the vicinity of cathode; however, it extended to the middle and even close to the anode over time. Due to the higher amount of charges at the cathode-dielectric interface and the accumulated positive charges close to the cathode, the electric field adjacent to the cathode enhanced up to 70 kV/mm, which is a 75% local field enhancement. With passing of time and change of the charge profile during the first cycle, the maximum electric field was reduced at the 90th minute before PR. For PR, the polarity of the bias was changed during 1 min with a constant ramp from +40 to -40 kV/mm. During and after PR, the charge distribution at the electrode-dielectric interfaces and the charge distribution in the bulk of the sample change. The PR is a transient condition that includes charge injection/extraction and recombination. Because of the higher amount of charges at the electrode-dielectric interface of the new anode after PR (the previous cathode with reversed polarity) compared with the new cathode (the previous cathode with reversed polarity) as well as transient charge distribution during 1 min PR, the electric field at the 91th min has been distorted significantly with a local enhancement up to 97 kV/mm, a 142.5% enhancement, next to the anode as depicted in Fig. 5(b). The charge distribution has changed over time during the second cycle

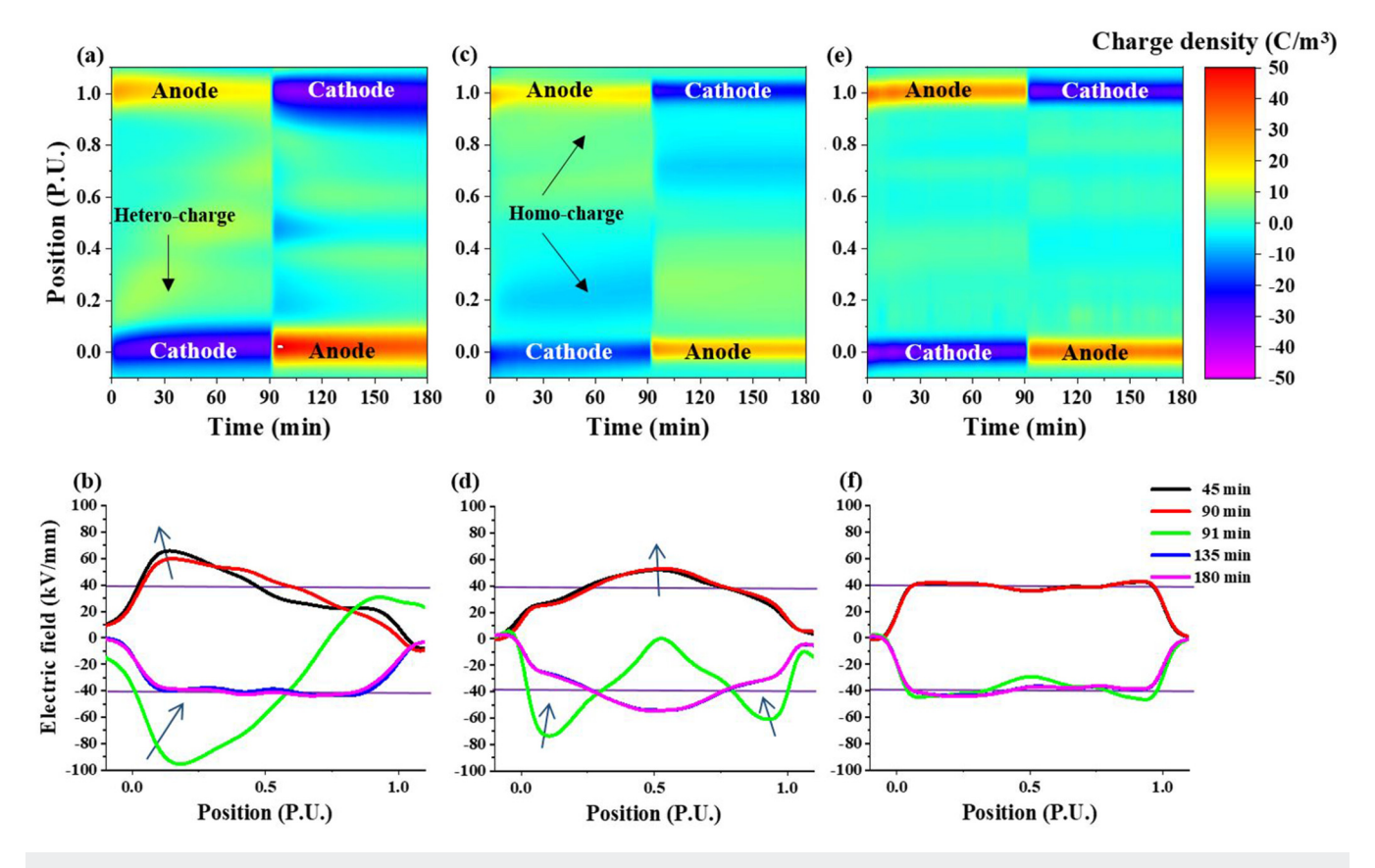


FIG. 5. Charge distribution profile and the resulted electric field distribution at 40 kV/mm and 50 °C with TG and polarity reversal for (a) and (b) EPR, (c) and (d) EPR-K, and (e) and (f) EPR-T.

over the second 90 min, and it was reduced and extended more uniformly across the sample. The decreased charge accumulation results in a notably uniform electric field across the EPR sample after 135 min.

EPR-K showed homo-polar charge accumulation during the first cycle of the applied electric field as shown in Fig. 5(c). Considering the evolution of charges at the electrode-dielectric interface, it is clear that the injected charges from the electrodes were captured as homo-polar charges during the transport across the sample under the electric field. As expected, this results in a local electric field enhancement up to 52 kV/mm, a 30% enhancement, in the middle of the sample, as shown in Fig. 5(d). During PR, because the evolution of charges at the electrode-dielectric interface is quicker compared with the bulk, the accumulated homo-polar charges before PR appeared as hetero-polar charges next to the charges at the electrode-dielectric interface at both electrodes. This condition distorts the electric field with a maximum electric field enhancement of 75 kV/mm, a 87.5% enhancement, next to the new cathode and 60 kV/mm, a 50% enhancement, near the new anode at the 91th minute after PR. Then, the homo-polar charges were redistributed under the new polarity, and therefore, the maximum electric field was shifted to the center of the sample similar to the condition before PR.

Figure 5(e) shows the charge distribution of EPR-T that could suppress charge accumulation notably compared with EPR and EPR-K such as the other two operational conditions. Some amount of accumulated charges can be seen; however, they did not distort electric field distribution significantly as shown in Fig. 5(f). In addition, during the PR for this sample, the transient local electric field enhancement is less than 45 kV/mm, which is only a 12.5% enhancement mainly because of the space charge suppression in the bulk.

#### D. Maximum charge density

Charge distribution along with electric field distribution can assess a dielectric more thoroughly. The reason is that if the dielectric captures successive layers or tiny clusters of positive and negative charges, electric field distribution is not significantly distorted, and consequently, the maximum electric field is not notably distorted with enhancement. However, the amount of absolute charges may still be large and accelerate the aging process of the sample through the storage of electromechanical energy. 13,27 Therefore, to quantify the amounts of accumulated charges across the bulk of the samples and have a clearer understanding in this context, the maximum of absolute amount of charge density across the bulk of dielectric during measurements was plotted. The maximum charge density was calculated in each acquisition of the charge profile and the charge at the electrode-dielectric interface including the capacitance charge induced by the polarization of the dielectric under the electric field and the surface charge induced by the accumulated space charge inside the bulk was not considered. Figure 6(a) shows the evolution of maximum charge densities (C/m<sup>3</sup>) during 120 min at 20 kV/mm at 25 °C as presented in Fig. 3. The maximum amount of charge density increases with time during the first 90 min for EPR and reached 3.6 C/m<sup>3</sup>, and after that it is more stable during the remaining time of measurement. The maximum amount of charge density in EPR-K has some changes in the first 20 min and then with an increasing rate it reaches from 0.5 to  $3.5\,\mathrm{C/m^3}$  at the 120th minute. The maximum charge density of EPR-T as expected based on previously explained results, as shown in Fig. 3, has a different trend compared with EPR and EPR-K. The maximum charge density increases to  $1.2\,\mathrm{C/m^3}$  in the first 5 min of measurement, and then, it is approximately stable during the entire measurement of 120 min with the amount of  $1.6\,\mathrm{C/m^3}$ .

The maximum value of charge density for the samples during 120 min at 20 kV/mm and 50 °C with TG is presented in Fig. 6(b). Similar to the previous condition, EPR has an increasing rate of maximum charge density that is more severe during the first 60 min and reaches up to  $5.2~\mathrm{C/m^3}$  at the end of measurement. The maximum amount of charge density for EPR-K also enhances quickly to  $2.5~\mathrm{C/m^3}$  during the first 30 min. After that, it reaches a more stabilized condition, while it still escalates to  $3.8~\mathrm{C/m^3}$  at the 120th minute. On the other hand, the maximum charge density of EPR-T reaches quickly the equilibrium of around  $1.12~\mathrm{C/m^3}$  during the initial 30 min and has only some small fluctuations during the remaining time of measurement.

Figure 6(c) shows the changes of maximum charge density during 180 min at 40 kV/mm and 50 °C with TG. For EPR, the maximum charge density fluctuates severely during the first cycle of measurement and raises up to 9.7 C/m³ at the 55th minute. During the PR, the maximum charge density inside the bulk decreases; however, exactly after PR, it reaches 10.6 C/m³. Then, during the next 30 min, it decreases sharply to about 4.9 C/m³, and it is stabilized at this amount up to the end of measurement. The maximum amount of charge density enhances quickly during the first 18 min and reaches equilibrium of 6.8 C/m³ in EPR-K during the first 90 min or the first cycle. During the PR, it reduces to 3.4 C/m³, and after that, it returns to the same value before PR. The maximum charge density of EPR-T gets to 2.8 C/m³ during the first 15 min, and then, it has some small variations between 2.2 and 2.9 C/m³ before and after PR.

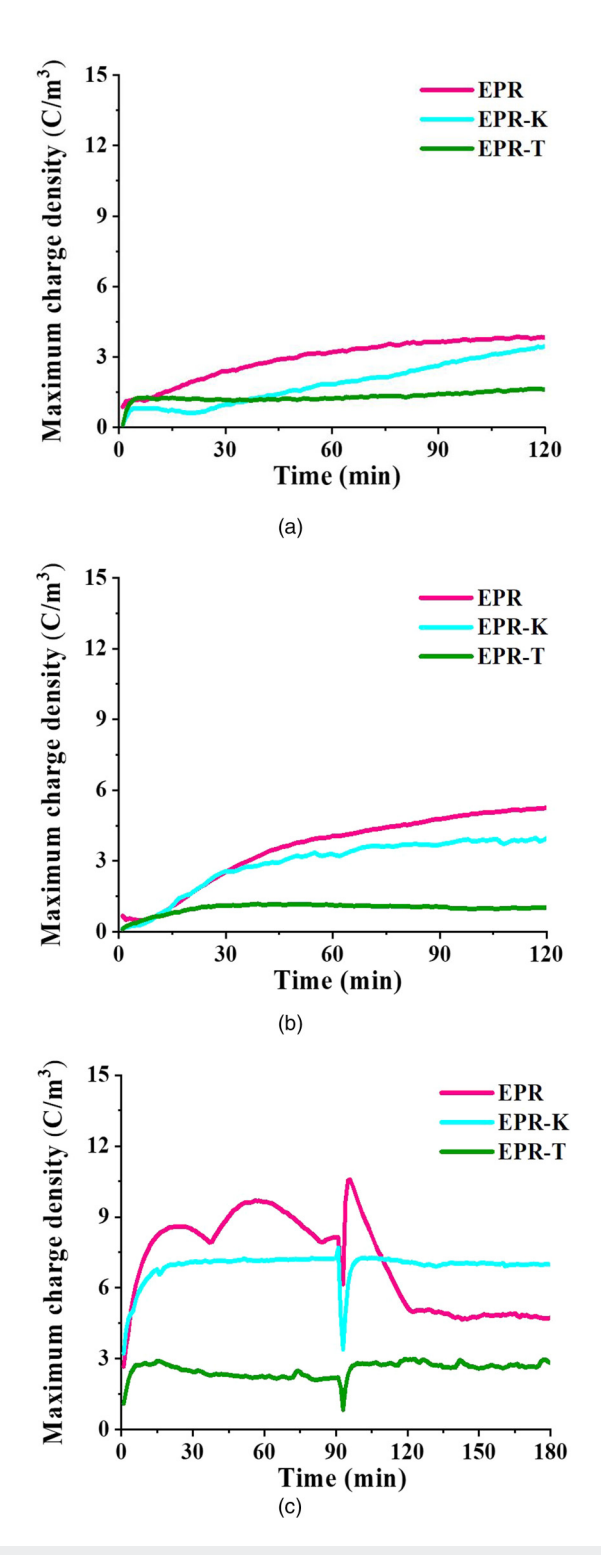
### E. Polarization and depolarization under 20 kV/mm at 25 $^{\circ}$ C

The charge density during  $120\,\mathrm{min}$  polarization under  $20\,\mathrm{kV/mm}$  and  $30\,\mathrm{min}$  short-circuited depolarization at  $25\,^\circ\mathrm{C}$  was measured, and the average charge density was calculated using Eq. (1) to help interpret the charge dynamics of the samples,

$$q(t) = \frac{1}{L} \int_{0}^{L} |q(x, t)| dx,$$
 (1)

where q(t) is the average of charge density (C/m³), L is the thickness (m), and q(x,t) is the charge at t at the position of x along the thickness (C/m³).<sup>28</sup>

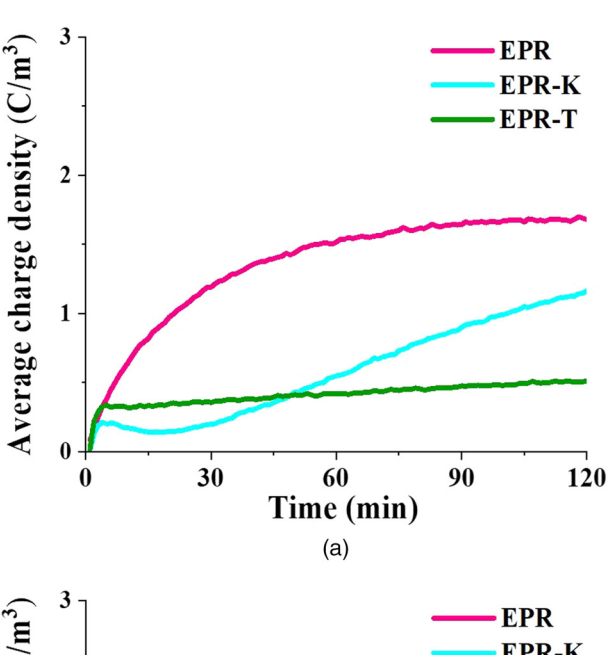
Figure 7(a) shows the average charge density during 120 min for the presented results in Fig. 3. EPR as expected from Fig. 3 has higher amount of average charge density of about 1.6 C/m<sup>3</sup>. The rate of charge density enhancement for EPR is significantly higher in the first 60 min compared with the second 60 min. EPR-K shows some small variations in the first 30 min and then with a sharp increasing rate gets up to 1.2 C/m<sup>3</sup> during the 120 min



**FIG. 6.** Maximum charge distribution for the three samples (a) at 20 kV/mm and 25 °C during 120 min, (b) at 20 kV/mm and 50 °C with TG during 120 min, and (c) at 40 kV/mm and 50 °C with TG and polarity reversal during 180 min.

measurement. In contrast, the average amount of charge density for EPR-T is significantly lower compared with those in EPR and EPR-K, and it stabilizes at about 0.4 C/m<sup>3</sup> quickly.

After 120 min polarization at 20 kV/mm and 25 °C, the samples were short-circuited for 30 min. The average amount of charge density is shown in Fig. 7(b). It can be seen that the charge density decreases quickly during the first 3 min for the three samples and the rate of charge decay is not notable during the remaining time of depolarization. Moreover, the other clear observation is the significant difference between the average amount of charge densities for the samples with the lowest average charge



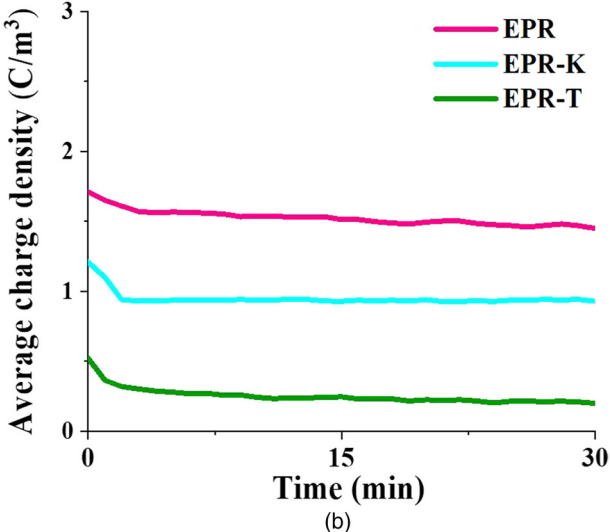
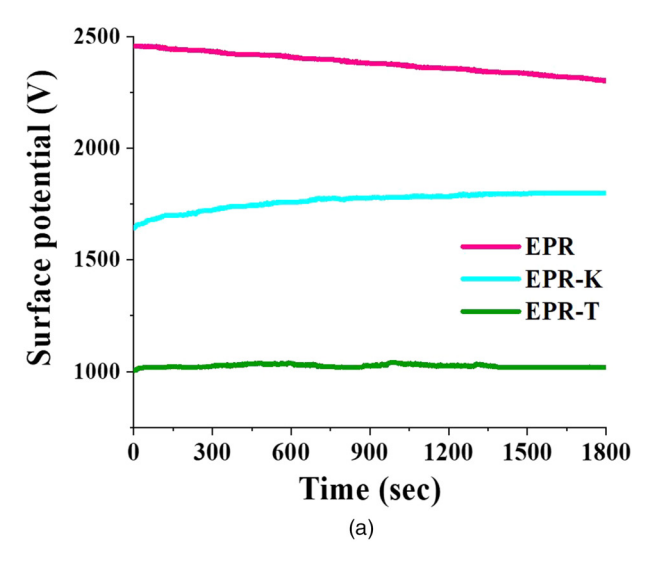


**FIG. 7.** Average charge density for the three samples (a) at  $20 \, \text{kV/mm}$  and  $25 \, ^{\circ}\text{C}$  during 120 min and (b) during 30 min short-circuit condition after polarization at  $20 \, \text{kV/mm}$  and  $25 \, ^{\circ}\text{C}$  for  $120 \, \text{min}$ .

density at about 0.19 C/m<sup>3</sup> for EPR-T at the end of 30 min compared with 1.46 C/m<sup>3</sup> for EPR and 0.93 C/m<sup>3</sup> for EPR-K.

#### F. Surface potential after polarization under 20 kV/mm

Space charge measurement during polarization and depolarization processes provides insights into the charge dynamics in the bulk of the samples. However, the surface potential is in relation with the amount of charge on the surface of dielectric or near the surface in the bulk. Therefore, the surface potential of the samples was measured in two scenarios to characterize the charge behavior more thoroughly. Figure 8(a) shows the surface potential of the



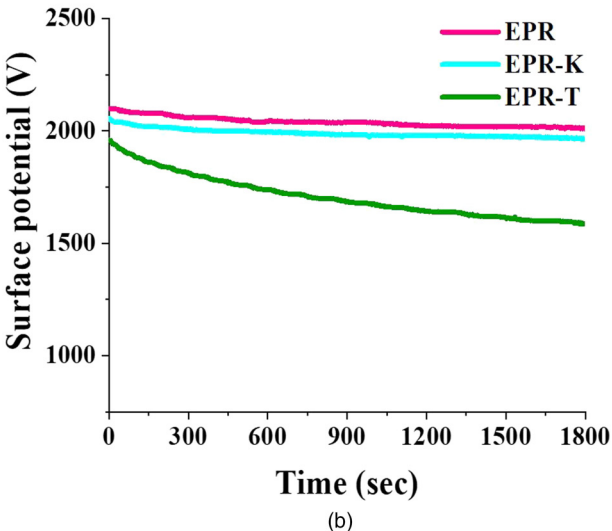


**FIG. 8.** Surface potential measurement during 1800 s for the three samples after (a) polarized at 20 kV/mm and 25 °C for 120 min and (b) charge with positive corona-discharge with 10 kV for 1 min.

samples during 30 min after 120 min polarization at 20 kV/mm at 25  $^{\circ}\text{C}$  (the first scenario).

The surface potential for EPR is higher compared with the ones in EPR-K and EPR-T and decreases during 30 min measurements from 2462 to 2306 V. The higher amount of surface potential for EPR is in relation to its higher amount of charge density during polarization. After disconnecting the applied voltage, the charge near the surface accounts for the initial surface potential. However, because of the recombination of accumulated hetero-polar charges close to the surface of EPR with charge at the interface, the amount of charges near the surface decreases, which consequently reduces the surface potential for the sample.

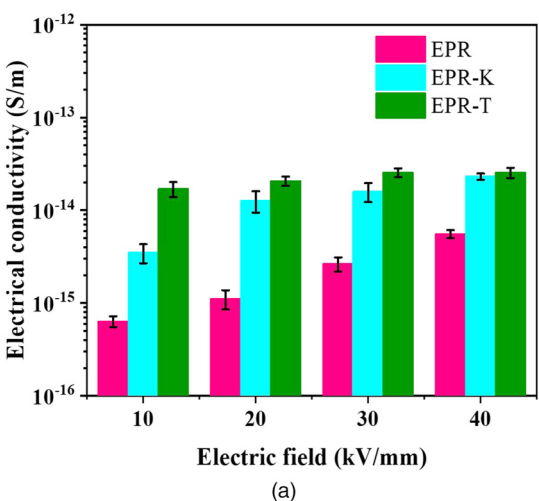
EPR-K has lower but increasing surface potential during the 30 min measurement, which enhances from 1647 to 1803 V. The amount of surface potential in EPR-K is also consistent with the charge accumulation for this sample. It seems that with voltage removal the accumulated homo-polar charges near the surface move toward the surface and it causes the increase in surface potential in EPR-K. EPR-T has a more stabilized surface potential, compared with EPR and EPR-K, with negligible variations between 1000 and 1023 V. The reason is that EPR-T has significantly suppressed charge accumulation, be it homo-polar or hetero-polar charge, and the amount of charges near the surface is negligible. Thus, the surface potential is low compared with EPR and EPR-K, and the amount of charges near the surface does not change after voltage removal.

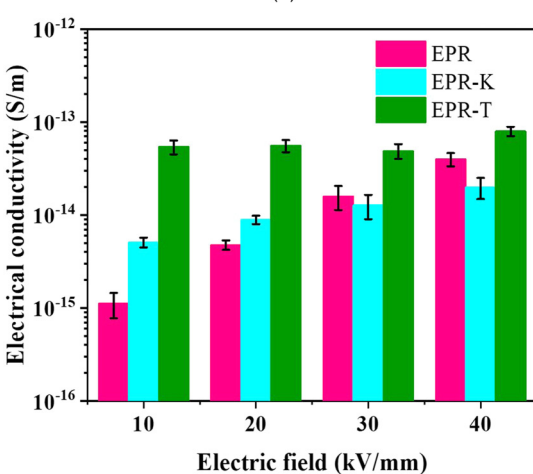
#### G. Surface potential after corona discharge

In the second scenario, the surface of the three samples was charged using positive corona-discharge for 1 min with 10 kV voltage. The distance between the tip of the high voltage needle and the surface of samples is 3 cm. The surface potential decay was measured for 30 min, and the results are shown in Fig. 8(b). The initial surface potential is in relation with the amount of charge carriers on the surface, <sup>25</sup> and it does not show a significant difference for the three samples. However, the amount of surface potential is lower for EPR-T compared with EPR and EPR-K. Moreover, the rate of surface potential decay is clearly different for the three samples. For EPR and EPR-K, the rate of decay is slow, and the surface potential does not change remarkably. In contrast, the surface potential reduces quickly from 1960 to 1581 V for EPR-T during the 30 min.

#### H. Electrical conductivity

The electrical conductivity of the samples under 10, 20, 30, and 40 kV/mm at 25, 50, and 90 °C is shown in Fig. 9. The plotted electrical conductivities are the average of three measurements for each sample under the determined electric field and temperature, and the error bars present the standard deviation of the results. The first observation is the obvious enhancement of electrical conductivity with increasing electric field and temperature. In this context, the electrical conductivity of the samples changes differently. For instance, electrical conductivity of EPR enhances markedly with an increasing electric field at measuring temperatures. However, the electrical conductivity of EPR-T has less variations with the electric field. To quantify the dependency of electrical





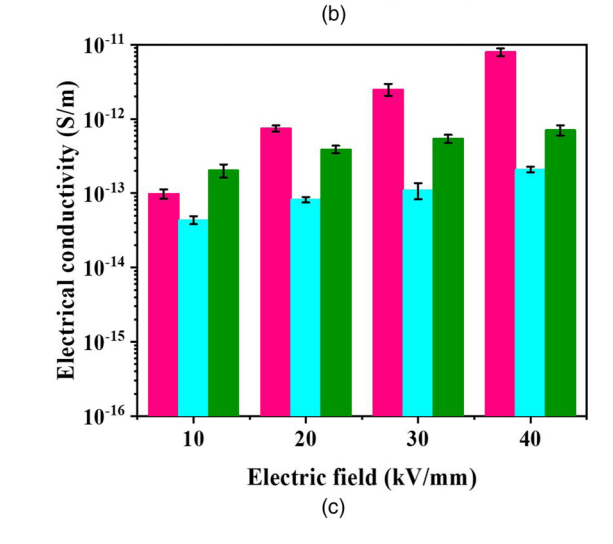


**FIG. 9.** Electrical conductivity of bulk for the three samples at (a) 25, (b) 50, and (c) 90  $^{\circ}$ C under 10, 20, 30, and 40 kV/mm.

conductivity on the electric field at a constant temperature, the exponential function was used as follows:

$$\sigma(E) = \sigma_0 e^{\alpha E},\tag{2}$$

where  $\alpha$  is the coefficient of electric field dependency of conductivity (mm/kV), E is the electric field (kV/mm),  $\sigma(E)$  is the conductivity as a function of E at a constant temperature (S/m), and  $\sigma_0$  is the conductivity at a constant temperature at E=0 (S/m). Table I presents the values of  $\alpha$  and  $\sigma_0$  obtained from fitting the experimental results with Eq. (2). It can be seen that  $\alpha$  is noticeably lower for EPR-T at measuring temperatures, compared with EPR and EPR-K. Furthermore, it is clear from the results that the dependency of conductivity on E grows with temperature rise. The other important observation from Fig. 9 and Table I is the higher electrical conductivity of EPR-T compared with EPR and EPR-K at 25 and 50 °C temperatures; however, because of its higher dependency to temperature, the electrical conductivity of EPR enhanced significantly at 90 °C, higher than both nanodielectrics.

#### I. Permittivity

Figure 10 shows the value of relative permittivity at different temperatures at a frequency of 0.01 Hz for the samples. It can be seen that the permittivity value for EPR is lower compared with EPR-K and EPR-T. In addition, the permittivity of the samples changes with temperature; however, the variations can be considered negligible compared with the variation of conductivity with the temperature and electric field. The permittivity of EPR, EPR-K, and EPR-T change in the range of 1.81–2.05, 2.71–3.04, and 2.71–3.20, respectively, which are less than 20% variation.

#### **IV. DISCUSSION**

Suppressing space charge accumulation in the bulk of dielectric under a DC electric field is one of the most desired characteristics of HVDC cable insulation. The measured results with the PEA method show the total charge distribution across the samples because of charge injection at the electrode–dielectric interface, ionization, and gradient of electrical conductivity in the bulk.<sup>29</sup> It is difficult if not impossible to discriminate the accumulated charges over different processes. The resulted charge distribution will define the electric field distribution across dielectrics, which is the

**TABLE I.** The obtained values for  $\alpha$  and  $\sigma_0$  at 25 and 50 °C.

Sample	Temperature (°C)	$\sigma_0$ (S/m)	α (mm/kV)
EPR	25	$2.64 \times 10^{-16}$	0.076
	50	$7.75 \times 10^{-16}$	0.098
	90	$7.22 \times 10^{-14}$	0.117
EPR-K	25	$4.29 \times 10^{-15}$	0.042
	50	$3.55 \times 10^{-15}$	0.043
	90	$2.54 \times 10^{-14}$	0.052
EPR-T	25	$1.57 \times 10^{-14}$	0.013
	50	$4.46 \times 10^{-14}$	0.014
	90	$1.78 \times 10^{-13}$	0.035

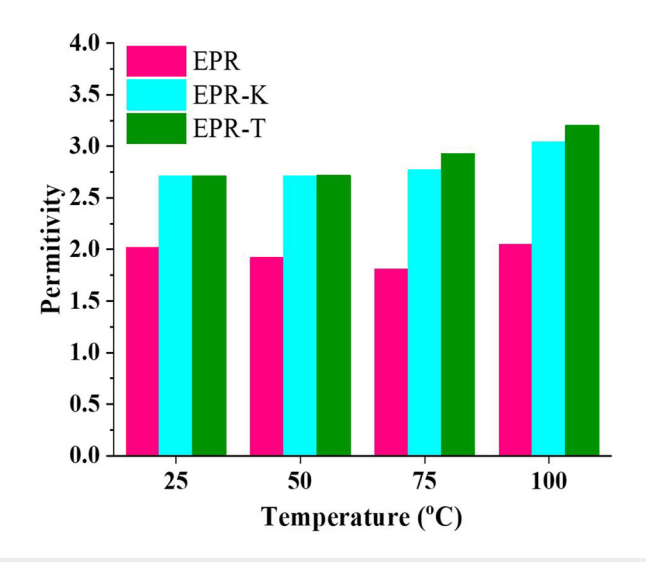


FIG. 10. Relative permittivity at frequency of 0.01 Hz at different temperatures for the three samples.

most critical parameter in the design of HVDC cable insulation. Presented results in this study show that EPR-T has an excellent performance in terms of space charge suppression and consequently electric field distribution in all investigated operational conditions including a normal electric field at 25 °C, a normal electric field with temperature rise and TG, and an enhanced electric field, 40 kV/mm, with temperature rise and TG with PR.

The results of electrical characterizations at 25 °C including polarization at 20 kV/mm, depolarization under short-circuit condition, and surface potential measurement after voltage removal were used to investigate charge dynamics in the studied model of the DC material and elaborate on the better performance of EPR-T compared with EPR and EPR-K. Figure 11 illustrates the schematic model that presents charge dynamics in the three samples. As described previously, EPR shows hetero-polar charge accumulation next to both electrodes presented in Fig. 11(a). The captured charges due to deep localized states appear as hetero-polar charges. The average and maximum of absolute amount of charges for EPR are significantly higher compared with EPR-K and EPR-T during 120 min polarization under 20 kV/mm and at 25 °C. After EPR was short-circuited, Fig. 11(b), a portion of charges trapped in the bulk was released during the first minutes. However, as previously presented in Fig. 7(b), the other portion of charges remain with small variations during the 30 min measurement and a low rate of recombination charge carriers captured by shallow localized states involved in the conduction process. In other words, the remaining charges in the bulk of samples are captured in deeper localized states and need more thermal energy to release. Based on the experimental results of surface potential measurement, in the case of voltage removal, EPR shows the decrease in surface potential. The recombination and neutralization of charges near the surface of EPR due to the de-trapping of accumulated hetero-polar charges and moving toward the surface as shown in Fig. 11(c) can explain this phenomenon.

Based on the experimental results, EPR-K accumulates charges as homo-polar charges near both electrodes as presented schematically in Fig. 11(d). The maximum and average of absolute amounts of charges in EPR-K are lower compared with EPR. After short-circuiting EPR-K shown in Fig. 11(e), similar to EPR, the charges from the shallow localized states are released while the deeper localized states still keep charge. Figure 11(f) shows charge distribution after voltage removal graphically for EPR-K. According to the results presented in Fig. 8(a), the surface potential of EPR-K enhances during the 30 min measurement because some trapped homo-polar charges near the surface were de-trapped and migrated to the surface of the sample.

The schematic charge profile of EPR-T with very low amount of accumulated charges across the bulk is presented in Fig. 11(g). Because the trapped charges are remarkably suppressed in EPR-T, the maximum and average amounts of charge density during polarization and short-circuit condition, Fig. 11(h), are greatly lower, compared with EPR and EPR-K. Moreover, since the amount of released charges is negligible and could not influence the charges near the surface of the sample, the surface potential of EPR-T does not change as shown in Fig. 11(i) during the 30 min measurement after voltage removal.

The distinct charge dynamics behavior in EPR, EPR-K, and EPR-T must be directly dependent on the distribution of localized states in the bulk of dielectric. As mentioned before, the electrical conductivity of EPR-T at both temperatures is higher than EPR and EPR-K. Electrical conductivity represents the macroscopic effect of charge carrier's mobility in dielectrics.<sup>30</sup> The higher charge carrier mobility at low temperatures should be the result of higher density of shallow localized states<sup>31</sup> in EPR-T when compared with EPR and EPR-K. Moreover, the lower  $\alpha$  or dependency of conductivity to the electric field implies the lower distance between the equilibrium states involved in charge transport.<sup>32</sup> Furthermore, in our previous study in Ref. 16, we showed that incorporation of 2D Talc nanoclay in EPR results in a significant reduction in activation energy and, thus, the average depth of localized states. Therefore, it is expected that the distribution of localized states in EPR-T includes higher density of shallower localized states compared with EPR and EPR-K. This decreases the possibility of trapping charges moving across the bulk and suppresses space charge accumulation.

Moreover, the lower dependency of electrical conductivity on the electric field and temperature reduces the space charge due to spatially inhomogeneous conductivity. The space charge formed under conductivity gradient can be calculated using the following equation:

$$\rho = -\frac{-\varepsilon_0 \varepsilon_r}{\sigma} \frac{\partial \rho}{\partial t} + \sigma E \cdot \nabla \left( \frac{\varepsilon_0 \varepsilon_r}{\sigma} \right), \tag{3}$$

where  $\rho$  is the generated space charge (C/m<sup>3</sup>),  $\sigma$  is the electrical conductivity (S/m), E is the electric field (V/m),  $E_r$  is the dielectric constant, and  $E_0$  is the permittivity of vacuum.<sup>33,34</sup> Accordingly, the lower dependency of electrical conductivity of EPR-T on the electric field and temperature could notably suppress the space charge.

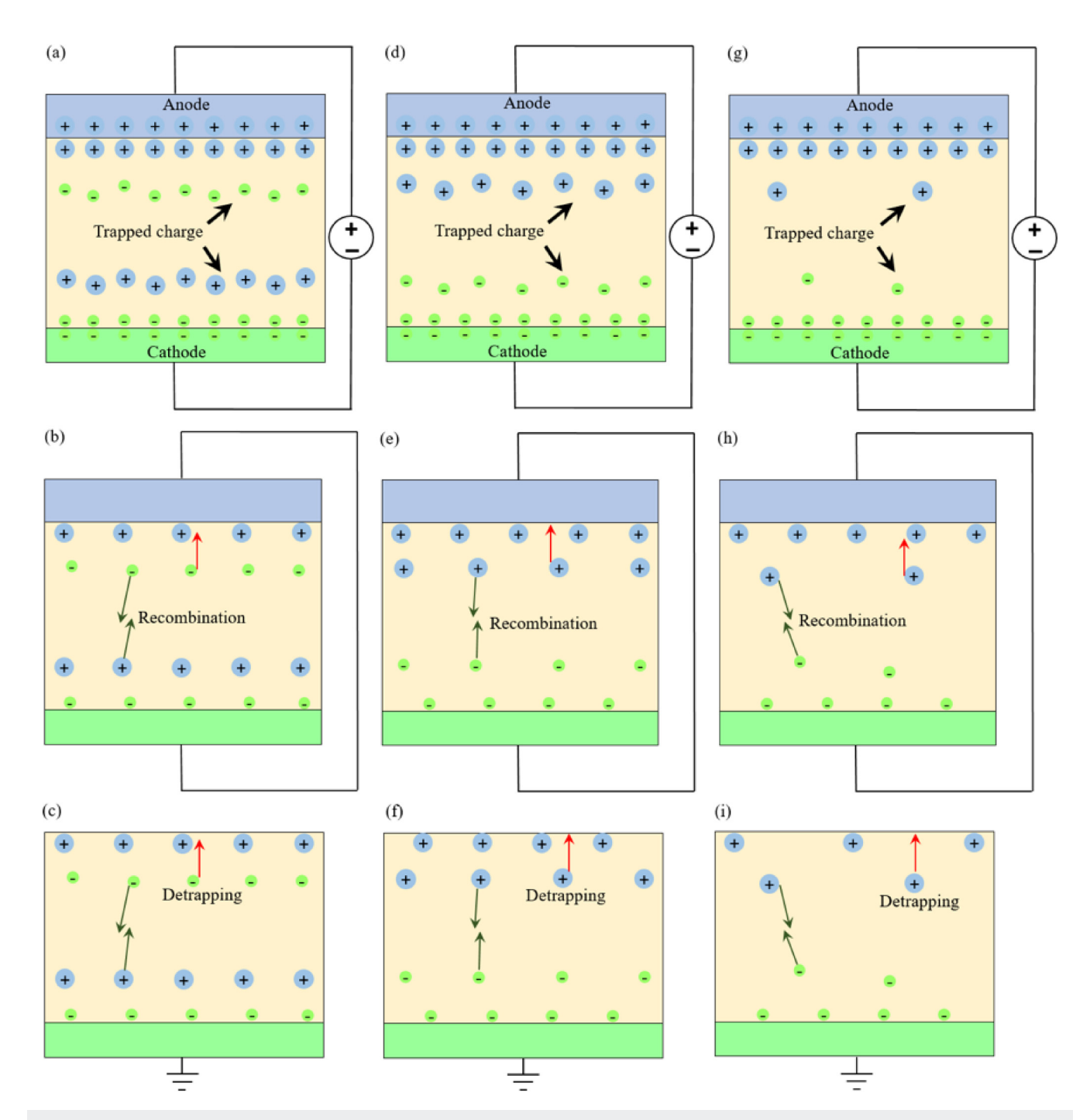


FIG. 11. Schematic presentation of charge dynamics under applied voltage, short-circuit, and voltage removal for (a)–(c) EPR, (d)–(f) EPR-K, and (g)–(i) EPR-T.

The other important parameter that should be considered carefully in the design of DC cable insulation is dielectric time constant  $(\tau = \varepsilon/\sigma)$ , which characterizes the relaxation time for dielectrics. <sup>7,10,33</sup> The lower dielectric time constant implies a

quicker redistribution of charges across the dielectric, which can prevent the large local electric field enhancement in transient condition of PR. Dielectric time constant is dependent on both permittivity and electrical conductivity. However, as mentioned before, the relative permittivity does not change notably with the temperature and electric field. Thus, the electrical conductivity is the leading parameter in defining time constant. The higher electrical conductivity of EPR-T at measured temperatures compared with EPR and EPR-K results in a lower time constant. Therefore, the redistribution of space charge across the bulk of EPR-T is quicker and can follow PR to prevent the transient electric field enhancement during and shortly after PR.

It should be mentioned that under fast transients, such as voltage impulse, because the occurrence time is sufficiently lower than time constant, a capacitive field grading will superimpose on the top of resistive field grading that can cause a maximum electric field higher than the maximum electric field in both capacitive and resistive field grading. The reverse polarity surge impulse and transient impulse were not characterized in this study; however, the PR with 1 min transient time that is in agreement with CIGRE TB 496 was characterized. As it is described in Fig. 5, EPR and EPR-K show a notable local electric field enhancement during and shortly after PR. On the other hand, EPR-T could control and tune the electric field during the studied PR condition not only because of the much more suppressed space charge, but also the lower dielectric time constant.

The higher limit of electrical conductivity in dielectrics designed for HVDC cable insulation is defined by power dissipation in dielectric.33 The conductivity must be low enough to prevent excessive heating and thermal runaway. To investigate the power dissipation condition in our studied model, we adopt the condition mentioned in Ref. 33 for a 150 kV HVDC power cable buried in depth of 2 m in the soil of thermal resistivity of 0.8 m K/W with an inner radius of 10 mm and an outer radius of 19 mm, which obtain  $Q = 2.0 \text{ kW/m}^3$ . Considering the worst operational condition at 40 kV/mm and 90 °C, the measured electrical conductivity for EPR, EPR-K, and EPR-T are  $7.9 \times 10^{-12}$ ,  $2.1 \times 10^{-13}$ , and  $7.1 \times 10^{-13}$  (S/m), respectively. The obtained power density  $(Q = \sigma E^2)$  at 40 kV/mm for EPR, EPR-K, and EPR-T are 12.64 kW/m<sup>3</sup>, 336 W/m<sup>3</sup>, and 1.13 kW/m<sup>3</sup>, respectively, which satisfy the upper limit of electrical conductivity constraint for EPR-K and EPR-T. The reason for higher electrical conductivity in EPR is the severe dependency of electrical conductivity of EPR on the electric field and temperature, which may incur the risk of thermal runaway of the cable system.

#### V. CONCLUSIONS

Charge dynamics in the EPR and the EPR-based nanodielectrics under different operational conditions of the HVDC cable system have been studied. The results show that the EPR-based nanodielectric with Talc nanoclay particles suppressed space charge accumulation significantly in the bulk under different operational conditions. For example, the maximum of absolute amounts of charge density decreases from 3.6 to 1.6 C/m³ under 20 kV/mm at 25 °C and from 10.6 to 2.9 C/m³ under 40 kV/mm with PR at 50 °C with TG. The space charge suppression in EPR-T would be because of the shallower average of localized states as well as the lower dependency of electrical conductivity on the electric field and temperature, which reduces the conductivity gradient. Due to the suppression of space charge in EPR-T, electric field distribution was

tuned in the bulk with the maximum electric field enhancement less than 7.5% under 20 kV/mm at 25 °C. Suppressed space charge and the lower dielectric time constant at the studied condition for PR are the main reasons of controlling the electric field during and after PR with only 12.5% electric field enhancement in EPR-T. Therefore, EPR-T is a promising nanodielectric for DC cable insulation.

#### **ACKNOWLEDGMENTS**

This work was supported by Kerite, Okonite, Electrical Cable Compounds, Lion Elastomers and ExxonMobil and partially by the National Science Foundation (NSF) under Grant No. 1650544 through the iUCRC Center for Novel High Voltage/Temperature Materials and Structures (NSF HVT). The authors thank JoAnne Ronzello, Dr. Chuanyang Li, and Dr. Chao Wu for help with the experimental setting-up.

#### **AUTHOR DECLARATIONS**

#### **Conflict of Interest**

The authors have no conflicts to disclose.

#### **Author Contributions**

Mohamadreza Arab Baferani: Data curation (equal); Formal analysis (equal); Investigation (equal); Validation (equal); Writing – original draft (equal). Tohid Shahsavarian: Investigation (equal); Resources (equal); Writing – review & editing (equal). Mattewos Tefferi: Data curation (equal); Investigation (equal); Methodology (equal). Qin Chen: Formal analysis (equal); Validation (equal); Writing – review & editing (equal). Yang Cao: Conceptualization (equal); Formal analysis (equal); Funding acquisition (equal); Investigation (equal); Methodology (equal); Project administration (equal); Resources (equal); Supervision (equal); Writing – original draft (equal); Writing – review & editing (equal).

#### **DATA AVAILABILITY**

The data that support the findings of this study are available from the corresponding author upon reasonable request.

#### **REFERENCES**

<sup>1</sup>H. Ye, F. Tobias, L. Xianzhang, L. Yi, Z. Mingyu, H. Zhengyi, W. Haitian, Z. Qikai, X. Ruoyu, and L. Duo, "Review on HVDC cable terminations," High Voltage 3(2), 79–89 (2018).

<sup>2</sup>M. Tefferi, Z. Li, Y. Cao, H. Uehara, and Q. Chen, "Novel EPR-insulated DC cables for future multi-terminal MVDC integration," IEEE Electr. Insul. Mag. 35(5), 20–27 (2019).

<sup>3</sup>G. Chen, M. Hao, Z. Xu, A. Vaughan, J. Cao, and H. Wang, "Review of high voltage direct current cables," CSEE J. Power Energy Syst. 1(2), 9–21 (2015).

<sup>4</sup>G. Mazzanti and M. Marzinotto, Extruded Cables for High-Voltage Direct-Current Transmission: Advances in Research and Development (John Wiley & Sons, 2013), Vol. 93.

<sup>5</sup>M. Jeroense, "HVDC, the next generation of transmission: Highlights with focus on extruded cable systems," IEEJ Trans. Electr. Electron. Eng. 5(4), 400–404 (2010).

- <sup>6</sup>T. Worzyk, Submarine Power Cables: Design, Installation, Repair, Environmental Aspects (Springer Science & Business Media, 2009).
- <sup>7</sup>H. Ghorbani, M. Jeroense, C.-O. Olsson, and M. Saltzer, "HVDC cable systems—Highlighting extruded technology," IEEE Trans. Power Deliv. **29**(1), 414–421 (2014).
- <sup>8</sup>M. A. Baferani, T. Shahsavarian, C. Li, M. Tefferi, I. Jovanovic, and Y. Cao, "Electric field tailoring in HVDC cable joints utilizing electro-thermal simulation: Effect of field grading materials," in *IEEE Electrical Insulation Conference* (EIC, 2020), pp. 400–404.
- <sup>9</sup>S. Qin and S. Boggs, "Design considerations for high voltage DC components," IEEE Electr. Insul. Mag. **28**(6), 36–44 (2012).
- <sup>10</sup>T. Christen, L. Donzel, and F. Greuter, "Nonlinear resistive electric field grading part 1: Theory and simulation," IEEE Electr. Insul. Mag. 26(6), 47–59 (2010).
- <sup>11</sup>X. Wang, N. Yoshimura, K. Murata, Y. Tanaka, and T. Takada, "Space-charge characteristics in polyethylene," J. Appl. Phys. 84(3), 1546–1550 (1998).
- <sup>12</sup>D. Fabiani, G. C. Montanari, C. Laurent, G. Teyssedre, P. H. F. Morshuis, R. Bodega, L. A. Dissado, A. Campus, and U. H. Nilsson, "Polymeric HVDC cable design and space charge accumulation.: Part 1: Insulation/semicon interface," IEEE Electr. Insul. Mag. 23(6), 11–19 (2007).
- <sup>13</sup>L. A. Dissado, G. Mazzanti, and G. C. Montanari, "The role of trapped space charges in the electrical aging of insulating materials," IEEE Trans. Dielectr. Electr. Insul. 4(5), 496–506 (1997).
- <sup>14</sup>G. Mazzanti and G. C. Montanari, "A comparison between XLPE and EPR as insulating materials for HV cables," IEEE Trans. Power Deliv. 12(1), 15–28 (1997).
- <sup>15</sup>Z. Lei, C. Li, R. Men, and J. He, "Mechanism of bulk charging behavior of ethylene propylene rubber subjected to surface charge accumulation," J. Appl. Phys. 124(24), 244103 (2018).
- <sup>16</sup>M. A. Baferani, C. Li, M. Tefferi, N. Wang, and Y. Cao, "Large improvement in DC electrical properties of EPDM with 2D platelet nanoclay," J. Phys. D: Appl. Phys. 54(47), 475304 (2021).
- <sup>17</sup>L. Zhang, M. M. Khani, T. M. Krentz, Y. Huang, Y. Zhou, B. C. Benicewicz, J. K. Nelson, and L. S. Schadler, "Suppression of space charge in crosslinked polyethylene filled with poly(stearyl methacrylate)-grafted SiO<sub>2</sub> nanoparticles," Appl. Phys. Lett. 110(13), 132903 (2017).
- Appl. Phys. Lett. 110(13), 132303 (2017).

  18B. Han, X. Wang, Z. Sun, J. Yang, and Q. Lei, "Space charge suppression induced by deep traps in polyethylene/zeolite nanocomposite," Appl. Phys. Lett. 102(1), 012902 (2013).
- <sup>19</sup>F. Tian, Q. Lei, X. Wang, and Y. Wang, "Effect of deep trapping states on space charge suppression in polyethylene/ZnO nanocomposite," Appl. Phys. Lett. 99(14), 142903 (2011).
- 20 T. Takada, Y. Hayase, Y. Tanaka, and T. Okamoto, "Space charge trapping in electrical potential well caused by permanent and induced dipoles for LDPE/MgO nanocomposite," IEEE Trans. Dielectr. Electr. Insul. 15(1), 152–160 (2008).

- <sup>21</sup>X. Huang, P. Jiang, and Y. Yin, "Nanoparticle surface modification induced space charge suppression in linear low density polyethylene," Appl. Phys. Lett. **95**(24), 242905 (2009).
- 22Q. Cheng, J.-W. Zha, J.-T. Zhai, D.-L. Zhang, X. Bian, G. Chen, and Z.-M. Dang, "Improved space charge suppression in PP/SEBS nanocomposites by controlling MgO nanoparticles with abundant surface defects," Appl. Phys. Lett. 115(10), 102904 (2019).
- <sup>23</sup>Y. Shi, L. Zhang, J. Zhang, H. Zhang, and Z. Yue, "Improved charge-discharge cycling durability of PVDF dielectrics with MgO nanofillers," Appl. Phys. Lett. 116(17), 172902 (2020).
- <sup>24</sup>M. A. Baferani, C. Li, T. Shahsavarian, J. Ronzello, and Y. Cao, "High temperature insulation materials for DC cable insulation—Part I: Space charge and conduction," IEEE Trans. Dielectr. Electr. Insul. **28**(1), 223–230 (2021).
- <sup>25</sup>C. Li, T. Shahsavarian, M. Arab Baferani, and Y. Cao, "Tailoring insulation surface conductivity for surface partial discharge mitigation," Appl. Phys. Lett. 119(3), 032903 (2021).
- <sup>26</sup>C. Wu, M. Arab, J. Ronzello, and Y. Cao, "Charge transport dynamics and space charge accumulation in XLPE composites with 2D platelet fillers for HVDC cable insulation," IEEE Trans. Dielectr. Electr. Insul. 28(1), 3–10 (2021).
- <sup>27</sup>T. T. N. Vu, G. Teyssedre, S. Le Roy, and C. Laurent, "Space charge criteria in the assessment of insulation materials for HVDC," IEEE Trans. Dielectr. Electr. Insul. 24(3), 1405–1415 (2017).
- <sup>28</sup>B. X. Du, C. Han, J. Li, and Z. Li, "Effect of voltage stabilizers on the space charge behavior of XLPE for HVDC cable application," IEEE Trans. Dielectr. Electr. Insul. 26(1), 34–42 (2019).
- <sup>29</sup>R. Su, K. Wu, L. A. Dissado, C. Cheng, S. J. Dodd, Z. Lv, L. Zhong, and X. Wang, "Investigation of effects of charge injection and intrinsic ionic carriers in low-density polyethylene and cross-linked polyethylene," J. Appl. Phys. 127(16), 165103 (2020).
- 30T. J. Lewis, "Charge transport in polyethylene nano dielectrics," IEEE Trans. Dielectr. Electr. Insul. 21(2), 497–502 (2014).
- <sup>31</sup>M. A. Baferani, C. Li, and Y. Cao, "Shallow trap mediated charge transport in polymer dielectrics for HVDC by incorporating 2D nanoclay," Appl. Phys. A 128(284), 1–8 (2022).
- <sup>32</sup>M. J. P. Jeroense and F. H. Kreuger, "Electrical conduction in HVDC mass-impregnated paper cable," IEEE Trans. Dielectr. Electr. Insul. 2(5), 718–723 (1995).
- <sup>33</sup>M. Tefferi, M. A. Baferani, H. Uehara, and Y. Cao, "The correlation and balance of material properties for DC cable insulation at design field," IEEE Access 8, 187840–187847 (2020).
- <sup>34</sup>D. Fabiani, G. C. Montanari, C. Laurent, G. Teyssedre, P. H. F. Morshuis, R. Bodega, and L. A. Dissado, "HVDC cable design and space charge accumulation: Part 3: Effect of temperature gradient," IEEE Electr. Insul. Mag. 24(2), 5–14 (2008).